Probing quantum puddles: nonlinear dynamics in superfluid film optomechanics

Raabe, L.D.

Chapter 3

Theory of superfluid optomechanics

3.

The research presented in this thesis concerns the motion of thin films of superfluid helium-4 and its interaction with light. Therefore, these key aspects are introduced in this chapter. We review the two-fluid model of superfluid helium [34–36], how this model predicts film thicknesses above the bulk fluid and the equations of motion resulting in surface waves in thin films called third sound [37]. The mechanical modes of these third sound waves when restricted to a circular geometry [28] and how the restoring van der Waals force enables direct coupling of these modes are presented. The optomechanical and photothermal driving of the superfluid film is compared and the requirements for mechanical lasing are discussed. The first part of this discussion is based on the excellent book Low-Temperature physics by Enss and Hunklinger [9].

3.1 Superfluid helium-4

The physics of superfluid helium has gained renewed interest in the past years through novel probing techniques using the interaction of electromagnetic radiation with the different types of sound supported by superfluid helium. The first kind of these optomechanics experiments used a microwave cavity filled with superfluid helium [23], while more recent approaches have used thin, self-assembled films on optical, micron-sized ring resonators to optically control third sound modes [25] and enable Brillouin lasing at ultra-low threshold powers [26].

3.

While helium-4 displays a phase transition from gas to liquid at a comparatively low temperature of about 4.2 Kelvin, it only enters its solid phase at exceedingly high pressures of above 30 bar. Cooling down helium-4 below 1 to 2 Kelvin at medium to low pressures leads instead to the emergence of a fourth phase, the superfluid phase, which displays a range of interesting and unusual behaviors (see figure 2.1). For example, the friction-less flow of superfluid helium through narrow channels and capillaries was first discovered in 1938 by Kapitza [30] and independently by Allen and Misener [31]. Since then, a range of experiments has probed properties of superfluid Helium like viscosity [30], heat transport [32] and sound propagation [9], which has led for example to the discoveries of the fountain effect [32] and various types of sound propagation in superfluid helium [57–61]. Shortly after the first experimental discovery of superfluid Helium the theoretical framework of the two-fluid model [35] was postulated, which was later expanded upon by Landau [62] and Feynman [36].

3.1.1 Two-fluid model

The two-fluid model describes superfluid helium **as if** it was a mixture of two fluids, one with the properties of normal phase liquid helium and one with the properties of helium completely in the superfluid phase. However, it is important to state that these two components cannot be physically separated and that it is not possible to say which helium atoms belong to which phase. In fact, the physical fluid is not a mixture of two fluids, but the description of the two-fluid model makes accurate predictions for a wide range of experiments [9].

The density of the whole liquid ρ is made up of the density of the superfluid phase ρ_s

and the density of the normal fluid phase ρ_n, such that

$$\rho = \rho_s + \rho_n. \tag{3.1}$$

It is also assumed that the total entropy and viscosity of the mixture is carried by the normal-fluid component [9]. At the onset of superfluidity, called the lambda point, the mixture is almost entirely normal fluid. As the temperature is decreased the density fraction of the superfluid phase increases until the entire liquid is almost exclusively superfluid [9]. We mainly consider the second case because our experiments are performed at 20 mK, far below the lambda point.

Using the velocity of the normal and superfluid component v_n and v_s, we can introduce the momentum density of mass flow per unit volume [9]:

$$\boldsymbol{j} = \rho_n \cdot v_n + \rho_s \cdot v_s, \tag{3.2}$$

which allows us to find a continuity equation using mass conversation:

$$\frac{\partial \rho}{\partial t} = -\nabla \boldsymbol{j}. \tag{3.3}$$

If we restrict ourselves to the low temperature case we can treat the effect of the normal-fluid viscosity as a higher-order effect, which can be neglected to first order. Considering superfluid helium then as an ideal fluid with only one velocity $\boldsymbol{v}$, one density ρ and a pressure p allows us to write down the Euler equation [9].

$$\frac{\partial \boldsymbol{j}}{\partial t} + \rho \boldsymbol{v} \cdot \nabla \boldsymbol{v} = -\nabla p \tag{3.4}$$

The second term on the left side of equation (3.4) can be neglected for small velocities, because it scales quadratically with velocity.

Taking the idea of an ideal fluid without dissipation by friction further, we can also assume that motion is reversible and therefore entropy is conserved [9]:

$$\frac{\partial(\rho S)}{\partial t} = -\nabla(\rho S\, \boldsymbol{v}_n), \tag{3.5}$$

where ρS is the entropy density and S is the entropy per unit mass.

To set up the equations of motion Landau proposed the following thought experiment [9, 62]. We imagine that we add a portion of purely superfluid phase to a mixture of the two liquid phases of helium at constant volume. The internal energy per unit mass will then change according to $\mathrm{d}U = T\mathrm{d}S - p\mathrm{d}V + \mu\mathrm{d}m$, where we already replaced the Gibbs Free Energy G per unit mass by the chemical potential μ. Given that we keep a constant Volume ($\mathrm{d}V = 0$) and that the superfluid flow can be reversed ($\mathrm{d}S = 0$), this equation reduces to $dU = \mu\mathrm{d}m$. This just describes a change of mass of the superfluid component, as expected from our action in the thought experiment, if we consider μ as potential energy of the superfluid component per unit mass. $-\nabla\mu$ is the corresponding force and using the second law of motion we find [9]:

$$\frac{\mathrm{d}\boldsymbol{v}_s}{\mathrm{d}t} = -\nabla\mu. \tag{3.6}$$

This means a gradient in chemical potential will result in a change in flow of the superfluid. From here the thermodynamic relation $\mathrm{d}\mu = -S\mathrm{d}T + \frac{1}{\rho}\mathrm{d}p$ and the fact that the total differential $\mathrm{d}\boldsymbol{v}_s$ and partial differential $\partial\boldsymbol{v}_s$ only differ by a quadratic term in velocity leads to the equation of motion [9].

3.

$$\frac{\partial\boldsymbol{v}_s}{\partial t} = S\nabla T - \frac{1}{\rho}\nabla p \tag{3.7}$$

3.1.2 Film thickness above bulk superfluid

Experiments have shown that bulk superfluid helium, initially contained in a beaker, will flow as a thin film up along the wall of the beaker and drop down from there, eventually emptying the beaker [63, 64]. This behavior opens opportunities to study thin superfluid films, but also brings a range of experimental challenges with it, like requiring a carefully closed box to contain the superfluid Helium within.

Theoretically this behavior can be explained by considering the chemical potential μ for each part of the helium: helium film μ_f, gas μ_g and bulk liquid μ_l. In the case of saturated vapor pressure, both gravity and van der Waals forces will also act on the film above the liquid [9]:

$$\mu_f = \mu_l + \mu_{\mathrm{grav}} + \mu_{\mathrm{vdW}} = \mu_g \tag{3.8}$$

Equation 3.6 requires that any gradient in chemical potential between superfluid film μ_f and the bulk liquid μ_l will result in a change in flow of the superfluid, which eventually eliminates this gradient. In the steady state gravity and van der Waals forces therefore have to cancel out $\mu_{\mathrm{grav}} + \mu_{\mathrm{vdW}} = 0$. By inserting $\mu_{\mathrm{grav}} = gz_0$ and

$\mu_{\text{vdW}} = -\alpha/d^3$ we find the film thickness d [9]

$$d = \sqrt[3]{\frac{\alpha}{g z_0}}, \tag{3.9}$$

where z_0 is the height above the bulk liquid and α is the Hamaker constant, which depends on dielectric properties of the material of the wall [9]. The devices presented in this thesis are made from silica, which has a Hamaker constant $\alpha = 2.6 \times 10^{-24}$ m^{5}s^{-2} [65, 66]. At a typical height of 4 cm of our experiment presented in chapter 4 the film thickness is expected to be about 18.8 nm.

We can make an additional interesting observation when considering heating a point on the wall by a temperature ΔT, while not changing the pressure in the film d$p = 0$. The thermodynamic relation d$\mu = -S$d$T + \frac{1}{\rho}$dp leads to a change in chemical potential $\Delta\mu = -S\Delta T$, which has to be added to the aforementioned equilibrium of chemical potentials

3.

$$\mu_{\text{grav}} + \mu_{\text{vdW}} + \Delta\mu = 0. \tag{3.10}$$

Therefore the film thickness at the heated point has a new equilibrium value:

$$d = \sqrt[3]{\frac{\alpha}{g z_0 - S\Delta T}} \tag{3.11}$$

Heating a part of the wall ($\Delta T > 0$) thus leads to a larger equilibrium film thickness at the heated position. This observation agrees well with equation 3.7, which states that the superfluid component will flow towards a heated region until any gradient in chemical potential μ is compensated.

3.1.3 Third sound

For thin films of superfluid helium the normal component is viscously clamped to the substrate material and only the superfluid component can move. This type of sound propagation is called third sound [37].

$\rho = \rho_n + \rho_s$ is the total density of helium with normal and superfluid component. We define $\mathbf{j}$ as the momentum density of mass flow per unit volume [9]:

$$\mathbf{j} = \rho_n v_n + \rho_s v_s, \tag{3.12}$$

with v_n and v_s being the velocity of normal/superfluid component.

Then mass conservation is expressed by the continuity equation [9].

$$\frac{\partial \rho}{\partial t} = -\nabla \mathbf{j} \tag{3.13}$$

For third sound, we can assume the normal fluid to be completely immobile ($v_n = 0$) and adopt the convention $v_s = c_3$ to indicate the speed of third sound $c_3$only. Additionally at the low temperatures of 20 mK we are working with $\rho_n \rightarrow 0$ and $\rho_s \rightarrow 1$. In this case we can consider the effect of superfluid flow to cause a local increase $\xi(x,t)$ of the film thickness d. Then equation 3.13 can be written as [9]:

$$\rho_s \frac{\partial \xi}{\partial t} = -\rho_s d \frac{\partial c_3}{\partial x}. \tag{3.14}$$

3.

The force driving the superfluid component in a 1 dimensional system can be expressed in terms of the chemical potential μ.

$$\frac{\mathrm{d}c_3}{\mathrm{d}t} = -\nabla \mu \tag{3.15}$$

And using the thermodynamic relation $\mathrm{d}\mu = -S\mathrm{d}T + \frac{1}{\rho_s}\mathrm{d}p$ we get [9]:

$$\frac{\partial c_3}{\partial t} = S\nabla T - \frac{1}{\rho_s}\nabla p. \tag{3.16}$$

For a third sound wave far away from the photothermal drive $\nabla T \approx 0$, so the first term vanishes [9]. The pressure p at a certain film height $d + \xi(x,t)$ can be expressed in terms of the restoring van der Waals force $F_{vdW} = 3\alpha/d^4$ as $p(x) = \rho F_{vdW}$. So equation 3.16 becomes [9]:

$$\frac{\partial c_3}{\partial t} = -F_{vdW}\frac{\partial \xi}{\partial x}. \tag{3.17}$$

We can now obtain a wave equation by taking the partial derivative with respect to time and with respect to x of equation 3.14 and 3.17 respectively and combining the result [9].

$$\frac{\partial^2 \xi}{\partial t^2} = dF_{vdW}\frac{\partial^2 \xi}{\partial x^2} \tag{3.18}$$

A solution to this wave equation is a plane wave of the form $\xi = \xi_0 \exp(\mathrm{i}\omega(t - x/c_3))$

Inserting this solution leads to the third sound velocity c_3 as a function of the film thickness [9].

$$c_3(d) = \sqrt{dF_{vdW}} = \sqrt{3\alpha/d^3} \tag{3.19}$$

This allows us to determine the film thickness by only measuring the speed of third sound as presented in chapter 5.

3.1.4 Third sound modes

As we have previously explored, the helium film is attracted to the substrate through the van der Waals force and lives thus in a potential

$$V(z) = -\frac{\alpha_{vdW}}{z^3}, \tag{3.20}$$

where z is a film thickness variation from the equilibrium set by the balance of van der Waals forces and gravity. For the purposes of this thesis the movement of helium can be restricted to the circular disk of an optical ring resonator with radius R. While the van der Waals potential clearly is nonlinear, in the small amplitude limit, the resonance amplitude profiles of the superfluid film take the form of drumhead modes described by Bessel modes $\eta_{m,n}$ for an (m,n) third sound mode as shown in figure 3.1 [28, 29]:

$$\eta_{m,n}(r,\theta) = A_{m,n} J_m \left(\zeta_{m,n}\frac{r}{R}\right)\cos(m\theta). \tag{3.21}$$

Here we use spherical coordinates r and θ. A is the mode amplitude, J_m the Bessel function of the first kind and order m and $\zeta_{m,n}$ is the root of the Bessel function, depending additionally on the boundary conditions. Free boundary conditions allow a varying film height at the boundary, but no flow across the boundary, whereas fixed boundary conditions keep the film height at the boundary unchanged, but allow flow across it. The mechanical mode frequency of the third sound mode Ω_M depends on the third sound speed c_3 as

$$\Omega_M = \frac{\zeta_{m,n}c_3}{R}. \tag{3.22}$$

It is important to note here that Bessel modes are not harmonics of each other like the solutions for a simple 1D potential well.

The film height deviation is then given by

$$h(r,\theta,t) = \eta_{m,n}(r,\theta)\sin(\Omega_M t + \phi_{m,n}). \tag{3.23}$$

The effective mass of such a Bessel mode in a thin film can be much larger than the

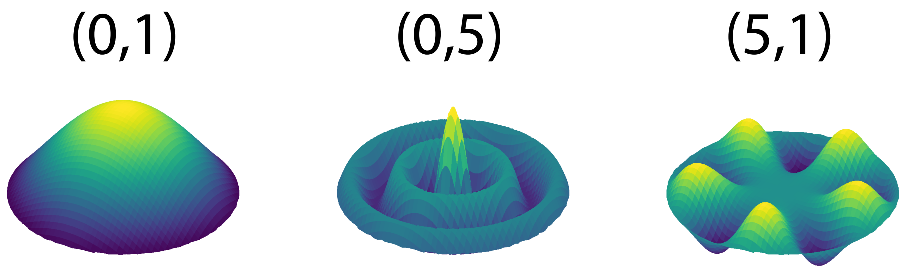

Figure 3.1: Bessel mode. Profile of 3 Bessel modes (m,n) with fixed boundary conditions.

total mass of the film. For the optomechanical interaction only the vertical movement of the film is considered. However, in shallow waves individual helium atoms have to move half a wavelength horizontally to enable the vertical film thickness variation. This movement dominates the overall motion of each individual helium atom for low order Bessel modes and is taken into account in the calculation of the effective mass [28]:

$$m_{\text{eff}} = 2\pi\rho\frac{R^2}{d}\frac{1}{\zeta^2}\frac{\int_0^R r\eta^2(r)dr}{\eta^2(R)}. \tag{3.24}$$

It is interesting to note that the effective mass for a circular third sound resonator scales as R^4/d, which enables to probe extremely large differences in effective mass $\mathrm{O}(10^{12})$ on a very similar platform by varying device sizes between $\mathcal{O}(\mu\mathrm{m})$ and $\mathcal{O}(\mathrm{mm})$ that can be fabricated with very high optical Q-factors [42, 47, 67]. The zero-point fluctuations of a mode Ω_M with effective mass m_{eff} is $x_0 = \sqrt{\frac{\hbar}{2m_{\text{eff}}\Omega_M}}$.

Turning back to equation 3.21, we can integrate the van der Waals potential over the entire surface deformation away from the film thickness d to find the stored potential energy [29]:

$$U = \rho\int_0^{2\pi}\int_0^R\int_d^{d+\eta(r,\theta)} V(z)r\ \mathrm{d}z\ \mathrm{d}r\ \mathrm{d}\theta \tag{3.25}$$

Using a Taylor series expansion

$$\int_d^{d+\eta(r,\theta)} V(z)\ \mathrm{d}z = \frac{\alpha_{\text{vdW}}}{2}\left(\frac{1}{(d+\eta(r,\theta))^2} - \frac{1}{d^2}\right) = \frac{\alpha_{\text{vdW}}}{2d^2}\sum_{j=0}^{\infty}(j+2)\left(-\frac{\eta(r,\theta)}{d}\right)^{j+1}, \tag{3.26}$$

one can rewrite the potential as a sum of quadratic, cubic and quartic potential energy terms [29]:

$$U = \rho \int_0^{2\pi} \int_0^R \left(\frac{3\alpha_{vdW}\eta^2}{2d^4} - \frac{2\alpha_{vdW}\eta^3}{d^5} + \frac{5\alpha_{vdW}\eta^4}{2d^6} \right) r \ \mathrm{d}r \ \mathrm{d}\theta \tag{3.27}$$

For a single Bessel mode one can introduce a reference point at the edge of the resonator $z = \eta(R, 0)$ to write the potential energy as [29]:

$$U(z) = \frac{1}{2}kz^2 + \frac{1}{3}\beta z^3 + \frac{1}{4}\alpha z^4. \tag{3.28}$$

The integrals for the pre-factors are explicitly evaluated in [29] and reveal the scaling $k \propto R^2/d^4$, $\beta \propto R^2/d^5$ and $\alpha \propto R^2/d^6$. In principle, in small geometries of $R < 1$ μm and low mechanical loss the higher order terms in the potential lead to a nondegenerate energy spectrum on the single phonon level, enabling direct control of individual occupation states [29]. However, for the large radius system presented in this thesis only large amplitudes lead to a noticeable influence of these terms.

For now our discussion has been limited to a single Bessel mode. However, many Bessel modes exist and may be driven on a circular geometry. We can therefore go back to equation 3.27 and ask what would happen if we consider a sum of Bessel modes. Relevant to our system is specifically a sum of purely radial Bessel modes $\sum_n \eta_{0,n}$. For the quadratic part of the potential the cross term of two Bessel modes cancels out, because they are orthogonal. However, the cubic potential introduces pair and triplet coupling between modes:

$$U(z_i, z_j, z_k) = \sum_i \frac{1}{2}k_i z_i^2 + \sum_i \frac{1}{3}\beta_i z_i^3 + \sum_{i \neq j} \beta_{ij} z_i^2 z_j + \sum_{\substack{j<k \\ j,k \neq i}} \beta_{ijk} z_i z_j z_k \tag{3.29}$$

Here β_{ij} and β_{ijk} are the overlap integrals resulting from equation 3.27. In practice, one highly driven mode may itself drive other modes out of equilibrium and even induce nonlinear effects such as small frequency changes. This gives rise to phenomena such as mode hopping of mechanical lasing states and mode-locked lasing of mechanical modes. The experimental realization is discussed in chapters 5 and 6.

Dispersion and nonlinearity

As discussed above, the mechanical modes on a disk are not frequency multiples of each other. A closer analysis of the dispersion law reveals an additional nonlinear contribution to the mechanical frequencies as a function of wavenumber $k = \frac{\zeta_{m,n}}{R}$ due to the nonlinear restoring van der Waals force and the addition of surface tension effects

$$\Omega_M(\lambda) = c_3 k + c_3 k^3 \left(\frac{\sigma d^4}{3\alpha\rho} - \frac{d^2}{3} \right), \tag{3.30}$$

where σ is the surface tension of superfluid helium, α is the aforementioned Hamaker constant and ρ is the density of superfluid helium [68]. However, for the low mode numbers used here the dispersion induces a negligible mode shift $\mathcal{O}(\text{mHz})$[1]. A closer inspection of equation 3.19 reveals that the speed of sound depends on the local film thickness and thus when a wave is excited the wave peaks will travel slower than the wave troughs. For a film thickness of 18.6 nm a wave with an amplitude of 1 nm will have a third sound speed difference of 20%. At large amplitudes this leads to the wave leaning backwards as it propagates and finally breaking backwards similar to how water waves lean and break forwards [69]. In a linear system dispersion and nonlinearity can cancel out, leading to the formation of a soliton pulse [68, 70, 71]. However, the dispersion required to offset the nonlinearity in this example would only happen at frequencies around 290 kHz. Instead, the direct mode coupling governed by equation 3.29 is much more relevant to the dynamics of our system.

3.2 Superfluid helium optomechanics

3.2.1 Optomechanical coupling

Similar to a FP cavity with a movable mirror (see chapter 2.2), an optical cavity mode will experience a change in its effective optical pathlength and therefore in its resonance frequencies ω if a medium with a relative permittivity $\epsilon_m > 1$ is overlapping with the electromagnetic field of that mode. The shift of the resonance frequency $\Delta\omega$ experienced by the optical cavity is proportional to the fraction of electromagnetic field $\vec{E}(\vec{r})$ overlapping with the medium [28].

[1]For a film thickness of 18.6 nm and a mode at 1 kHz we compute a shift of 2.2 mHz

$$\frac{\Delta\omega}{\omega} = -\frac{1}{2}\frac{\int_{\text{medium}}(\epsilon_m - 1)|\vec{E}(\vec{r})|^2 d^3\vec{r}}{\int_{\text{all}}\epsilon(\vec{r})|\vec{E}(\vec{r})|^2 d^3\vec{r}}. \tag{3.31}$$

Note that the integral in the numerator is taken over the volume of the medium, whereas the integral in the denominator is taken over the entire considered space. In this thesis, we work with a circular resonator microfabricted from silica and supporting optical whispering gallery modes (WGM). The evanescent field of the optical modes supported by these ring resonator extend hundreds of nanometers out of the material. When the device is coated uniformly with a thin film of superfluid helium there is thus a significant overlap of the superfluid helium film with the optical mode. For typical film thicknesses of 10 nm to 20 nm we can consider the evanescent electromagnetic field to be approximately constant, allowing us to calculate the optomechanical resonance frequency shift per film thickness displacement G [28]

3.

$$G = \frac{\Delta\omega}{\Delta z} = -\frac{\omega_0}{2}\frac{\int_{\text{superfluid}} q(\epsilon_{sf} - 1)|\vec{E}(\vec{r})|^2 d^2\vec{r}}{\int_{\text{all}}\epsilon(\vec{r})|\vec{E}(\vec{r})|^2 d^3\vec{r}}, \tag{3.32}$$

where the integral in the numerator and the denominator changed to be 2 dimensional due to the rotational symmetry of the considered geometry and we introduced the superfluid displacement profile $q = \frac{\eta(r)}{\eta(R)}x_0$. By optimizing the geometry of the resonator the overlap of the evanescent electromagnetic field with the superfluid film can be maximized to reach optomechanical coupling values of up to $G = -6$ GHz/nm [28]. However, optimizing the geometry with the sole purpose of maximizing G may come at the expense of the quality factor of the optical resonator. To achieve optimal single-photon optomechanical coupling strengths g_0 one has to take into account both of these factors, among other restrictions. Finite element modeling can help in finding optimal geometries through simulation.

COMSOL simulations

We use the electromagentic waves package of COMSOL multiphysics to simulate the optomechanical coupling G for our device geometry. We set up a 2D rotational symmetric simulation in the frequency domain and build the device geometry out of silica. We then solve for eigenfrequencies around 286 THz, which corresponds to our laser wavelength of 1064 nm. In this way, we can find the fundamental and higher order optical modes supported by the device. We add a thin layer of thickness d around the device geometry and give it the refractive index of liquid helium $n_{\text{He}} = 1.026$. We then

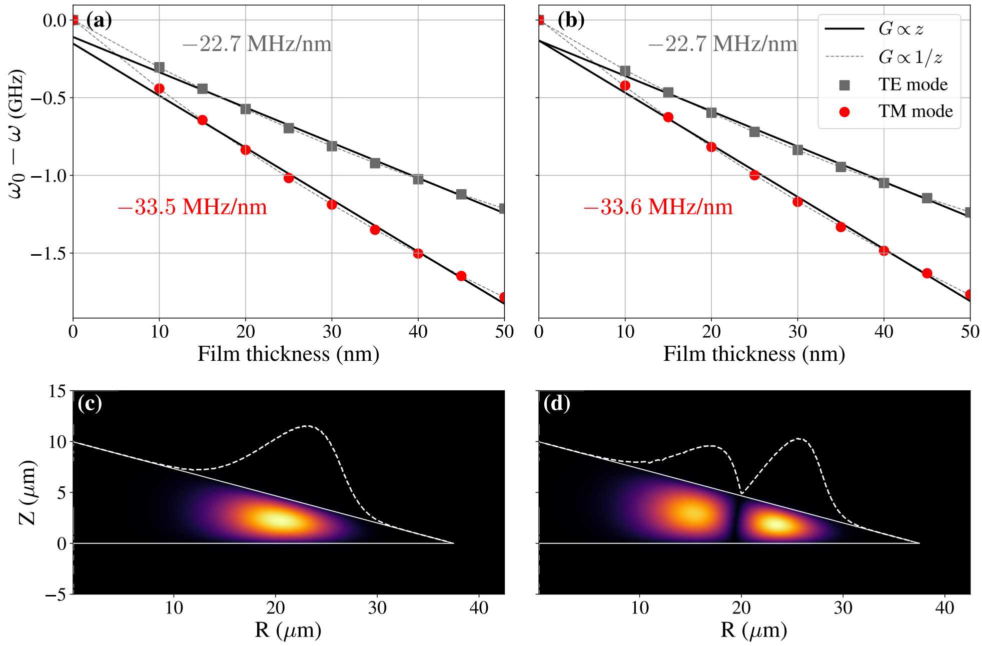

Figure 3.2: FEM simulation of the optical mode. (a),(b) Calculated frequency shifts of the fundamental optical mode and the (0,1) optical mode. **(c), (d)** Simulated optical mode profiles for the fundamental optical mode and the (0,1) optical mode. Dashed white lines indicate the relative electric field strength at the silica boundary. COMSOL simulations by Hidde Kanger.

set up a parametric sweep that sweeps the film thickness d between 0 and 50 nm and simulates the supported optical modes of the assembly for each film thickness. Figure 3.2 shows the red-shift of the TE and TM polarization of the fundamental and (0,1) optical modes. We find a roughly linear frequency shift per nm of superfluid helium of $G_{TM} = -33.5 \pm 0.1$ GHz/nm for the TM polarization and $G_{TE} = -22.7 \pm 0.1$ GHz/nm for the TE polarization. The frequency shift per nm G will only become nonlinear for much thicker film thicknesses on the order of the mode extension out of the material. Interestingly, the frequency shift is much more dependent on the polarization than on the mode number. We confirmed this trend also for higher order optical modes.

3.2.2 Photothermal driving

While we have seen above that there is direct optomechanical coupling between superfluid helium and light, superfluid helium also reacts strongly to heat through the superfluid fountain effect. The photothermal force is an indirect optomechanical coupling that takes into account the effect on a mechanical oscillator by heat generated through optical absoprtion. It has been shown theoretically that efficient ground-state cooling using photothermal forces is possible [72], opening the possibility for single phonon and superposition experiments. The classical equations of motion of a superfluid third sound mode with frequency Ω_M and amplitude z that interacts with the light circulating in a cavity can be written as

$$m_{\text{eff}}\ddot{z} + m_{\text{eff}}\Gamma_m\dot{z} + m_{\text{eff}}\Omega_M^2 z + O(z^2) = F_{RP} + F_{PT} + F_{th}, \tag{3.33}$$

where m_{eff} is the effective mass of the third sound mode and Γ_m is the mechanical damping. The radiation pressure force F_{RP}, the photothermal force F_{PT} and the thermal bath F_{th} act on the system.

3.

We have seen in chapter 2.3 that the radiation pressure force can be written as

$$F_{RP}(t) = \hbar G a^*(t)a(t), \tag{3.34}$$

where $a(t)$ is the complex electromagnetic field inside the optical resonator at the position of the optomechanical interaction. We can express the photothermal force as [73]

$$F_{PT}(t) = \frac{\beta G}{\tau_{th}} \int_{-\infty}^{t} e^{-\frac{t-u}{\tau_{th}}} a^*(u)a(u)du, \tag{3.35}$$

where β is a dimensionless factor that quantifies the ratio of photothermal and radiation-pressure force taking into account the absorption coefficient and the mode overlap with the heated region. τ_{th} is the thermal response time of the system. The integral in the expression acts effectively as a low pass filter that suppresses the photothermal force for processes faster than τ_{th}. For a constant or slowly varying intra-cavity power the radiation pressure and photothermal forces are proportional $F_{PT} = \beta F_{RP}$. Sawadsky et. al [73] developed a framework to simulate the ratio of photothermal and radiation pressure force by modeling the system as a combination of a thermal circuit and an RLC circuit. Specific system parameters, for example for different geometries and associated heat flows, are first obtained by using existing data and finite-element modeling. Simulation of the equivalent circuit then yields a photothermal response that can be compared to the radiation pressure. We have repeated this simulation for our main experimental platform, a wedge ring resonator with an undercut of 100 μm and a radius of 3 mm, for different temperatures and mechanical resonance frequencies (see figure 3.3). This yields a ratio of up to $\beta \approx 5 \times 10^7$. While there are significant uncertainties associated with this simulation, we can assume the photothermal force F_{PT} to be orders of magnitude larger than the radiation pressure force F_{RP} and can therefore neglect the latter in the following discussion. We will also discuss driving the film far away from its equilibrium state at very low temperatures and can thus ignore the thermal bath contributions F_{th}.

Photothermal heating is generally evenly distributed along the periphery of an optical ring resonator. This means that only purely radial Bessel modes $\eta_{0,n} = A_{0,n} J_0 \left(\zeta_{0,n} \frac{r}{R}\right)$ can be efficiently driven by photothermal forces. Driving of angular modes cancels out due to the angular symmetry of the driving force. Instead these modes have to be addressed by optomechanical scattering processes, such as Stokes and anti-Stokes photons [21] or Brioullin backscattering [26, 74, 75].

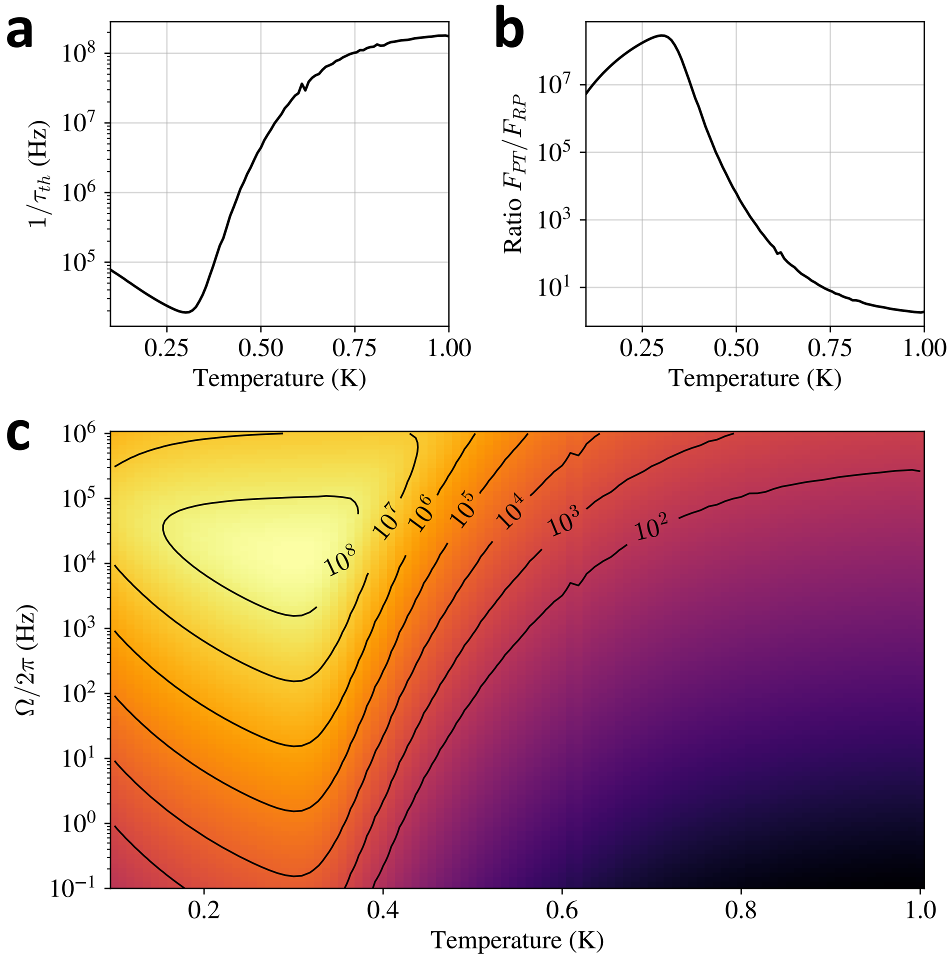

Figure 3.3: Ratio of photothermal and radiation pressure force $\mathbf{F_{PT}/F_{RP}}$ for a wedge ring resonator with a radius of 3 mm. **(a)** Simulation result for the frequency $1/\tau_{th}$ at which the photothermal force starts dropping off. **(b)** Simulation results for the ratio of the photothermal and radiation pressure force F_{PT}/F_{RP} as a function of the bath temperature for a mechanical mode frequency of $\Omega_M/2\pi = 5$kHz. **(c)** Simulation results for the ratio of the photothermal and radiation pressure force F_{PT}/F_{RP} for a range of temperatures and mechanical mode frequencies. Simulations by Hidde Kanger.

We can now consider an optical cavity with a cavity resonance frequency ω_c, a total damping rate κ, an external coupling rate κ_{ext} and a Finesse $\mathcal{F}$. A laser with a frequency ω_L and Power P_{in} will have an optical detuning $\Delta\omega = \omega_c - \omega_L$ with respect to the cavity, leading to a circulating intracavity power

$$P_{circ} = \mathcal{F}\frac{\kappa\kappa_{ext}}{(\kappa/2)^2 + \Delta\omega^2}P_{in}. \tag{3.36}$$

A change in thickness x of the superfluid Helium film at the position of the optical mode will lead to a change in the cavity frequency $\Delta\omega_c = G\Delta x$. In this way the detuning will effectively change to $\Delta\omega + G\Delta x$. In our experiment the optical damping rate is much bigger than the mechanical mode frequency $\kappa \gg \Omega_M$, which allows us to treat the circulating optical power as a steady state for each time step of a mechanical oscillation.

3.

$$P_{circ}(t) = P_{circ,0} + P_{circ,mod} = \frac{\mathcal{F}\kappa\kappa_{ext}}{\kappa^2 + \Delta\omega^2}P_{in} + \frac{\mathcal{F}\kappa\kappa_{ext}}{\kappa^2 + (\Delta\omega + Gze^{-i\Omega_M t})^2}P_{in}, \tag{3.37}$$

where z is the amplitude of the mechanical oscillation.

3.2.3 Mechanical lasing threshold

Our system resides deep within the unresolved sideband regime due to a small mechanical frequency $\Omega_M = \mathrm{O(kHz)}$ compared to the optical linewidth of our cavity $\kappa = \mathrm{O(MHz)}$. We therefore have to consider Stokes a_- and anti-Stokes a_+ scattering to fall into the same cavity resonance as the pump a_p [76]. The pump is detuned from the cavity frequency ω_c by $\Delta\omega = \omega_p - \omega_c$ Using the rotating wave approximation for the cavity frequency ω_c and the slowly varying envelope approximation, we can write down the following rate equations for the mechanical mode amplitude z and the optical field amplitudes a_p, a_+, a_-^*:

$$\frac{dz}{dt} = -\frac{\Gamma_m}{2}z - i\frac{\beta G x_0}{2}(a_p^* a_+ + a_p a_-^*) \tag{3.38}$$

$$\frac{da_p}{dt} = (-\frac{\kappa}{2} + i\Delta\omega)a_p - i\frac{Gx_0}{2}(z^* a_+ + z a_-) + \sqrt{\kappa_{ext}}s \tag{3.39}$$

$$\frac{da_+}{dt} = -\frac{\kappa}{2}a_+ + i(\Delta\omega + \Omega_M) - i\frac{Gx_0}{2}z a_p \tag{3.40}$$

$$\frac{da_-^*}{dt} = -\frac{\kappa}{2}a_- - i(\Delta\omega - \Omega_M)a_-^* + i\frac{Gx_0}{2}z a_p^*, \tag{3.41}$$

where we introduce the damping terms Γ_m and $\kappa = \kappa_{int} + \kappa_{ext}$ of the mechanical and optical mode as well as an external driving field s of the optical mode. G is the frequency shift per displacement of superfluid height and x_0 is the zero-point fluctuation of the mechanical mode. The photothermal driving of the mechanical mode in equation 3.38 is enhanced by a factor β with respect to the standard optomechanical interaction. While the photothermal response function in general is more complicated, this approach is valid for mechanical dynamics that are significantly slower than the thermal response time of the system.

We can solve the coupled equations in the steady state of the optical fields.

$$a_p = -\frac{iGx_0(z^* a_+ + z a_-) + \sqrt{\kappa_{ext}} s}{2(-\kappa/2 + i\Delta\omega)} \tag{3.42}$$

$$a_+ = -\frac{iGx_0}{2(-\kappa/2 + i(\Delta\omega + \Omega_M))} z a_p \tag{3.43}$$

$$a_-^* = -\frac{iGx_0}{2(-\kappa/2 - i(\Delta\omega - \Omega_M))} z a_p \tag{3.44}$$

3.

Plugging these results into equation 3.38 and only keeping the real part yields

$$\frac{dz}{dt} = -\frac{\Gamma_m}{2} z + \frac{1}{8} \frac{\beta G^2 x_o^2 \kappa |a_p|^2}{\frac{\kappa^2}{4} + (\Delta\omega - \Omega_M)^2} z - \frac{1}{8} \frac{\beta G^2 x_o^2 \kappa |a_p|^2}{\frac{\kappa^2}{4} + (\Delta\omega + \Omega_M)^2} z. \tag{3.45}$$

We can replace the intracavity power $|a_p|^2$ with the input power P_{in} by neglecting the optomechanical interaction for small amplitudes z

$$|a_p|^2 = \frac{\kappa_{ext}}{\frac{\kappa^2}{4} + \Delta\omega^2} \frac{P_{in}}{\hbar\omega}. \tag{3.46}$$

The onset of mechanical lasing starts when the overall damping of the mechanical motion becomes positive, which leads to the lasing threshold power

$$P_{in,thresh} = \hbar\omega \frac{4\Gamma_m}{\beta G^2 x_0^2} \frac{\frac{\kappa^2}{4} + \Delta\omega}{\kappa\kappa_{ext}} \left[\frac{1}{\frac{\kappa^2}{4} + (\Delta\omega - \Omega_M)} - \frac{1}{\frac{\kappa^2}{4} + (\Delta\omega + \Omega_M)} \right]^{-1}. \tag{3.47}$$

The last term of this equation allows for a positive threshold power if $\Delta\Omega > 0$ (blue detuning). For $\Delta\Omega < 0$ (red detuning) the mechanical mode is cooled. However, in the most general case the photothermal force is complex, which can allow for mechanical lasing on the red detuned side.

3.3 Multimode optomechanics

As we have previously discussed a thin film of superfluid helium confined to a circular geometry supports many different Bessel modes with complex amplitude z_i. The optomechanical coupled mode equations therefore become

$$\ddot{z}_i = -\Gamma_m \dot{z}_i - \Omega_M^2 z_i + \beta_i z_i^2 + \sum_{i \neq j} \beta_{ij} z_i z_j + \sum_{\substack{j<k \\ j,k \neq i}} \beta_{ijk} z_j z_k + \frac{\hbar \beta_i G}{m_{eff,i} \tau_{th}} \int_{-\infty}^{t} e^{-\frac{t-u}{\tau_{th}}} a^* a \tag{3.48}$$

$$\frac{da_p}{dt} = (-\frac{\kappa}{2} + i\Delta\omega) a_p - i\frac{Gx_0}{2} \left(\sum_i z_i^* a_+ + \sum_i z_i a_- \right) + \sqrt{\kappa_{ext}} s \tag{3.49}$$

$$\frac{da_+}{dt} = -\frac{\kappa}{2} a_+ + i(\Delta\omega + \Omega_M) - i\frac{Gx_0}{2} \sum_i z_i a_p \tag{3.50}$$

$$\frac{da_-^*}{dt} = -\frac{\kappa}{2} a_- - i(\Delta\omega - \Omega_M) a_-^* + i\frac{Gx_0}{2} \sum_i z_i a_p^*. \tag{3.51}$$

3.

Introducing another variable $v_i = \dot{z}_i$ allows to turn this set of equations into a set of coupled ordinary differential equations (ODE) that can be efficiently numerically simulated using methods such as Runge-Kutta.

3.4 Conclusion

In this chapter I have given a summary of the two fluid model of superfluid helium and how a range of interesting and experimentally verified phenomena arise from this treatment. A particular focus was put on the formation of thin films of superfluid Helium and the associated third sound. If these films are condensed on top of an optical whispering gallery mode resonator, a red shift of the optical resonance occurs leading to optomechanical coupling. The confinement of the film on a circular geometry leads to the rise of mechanical modes. Due to the nonlinear restoring van der Waals force, higher order terms lead to direct coupling of these Bessel modes. Photothermal driving of these films can display orders of magnitude stronger effects than radiation pressure forces, leading to a largely reduced mechanical lasing threshold.

Acknowledgments

I thank Martin van Exter for useful discussions on the optomechanical interactions between light and superfluid helium. I also thank Hidde Kanger for his contribution to the simulations of the photothermal force in our system.

3.

3.